Applied Thermal Engineering 236 (2024) 121455

Contents lists available at ScienceDirect

Applied Thermal Engineering

journal homepage: www.elsevier.com/locate/ate

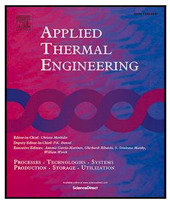

Research Paper

Numerical study of an ultrasonic spray atomiser as an evaporative cooler

P. Navarro [a], J. Ruiz [b,*], P. Martínez [b], M. Lucas [b]

[a] Departamento de Ingeniería Térmica y de Fluidos, Universidad Politécnica de Cartagena, Dr. Fleming, s/n, 30202 Cartagena, Spain
[b] Departamento de Ingeniería Mecánica y Energía, Universidad Miguel Hernández, Avda. de la Universidad, s/n, 03202 Elche, Spain

ARTICLE INFO

Keywords:
CFD
Cooling efficiency
Ultrasonic atomiser
Evaporative cooling

ABSTRACT

Pre-cooling the inlet air of an air conditioning condenser through evaporative cooling has proven highly effective in enhancing performance. Previous works focused on utilising an ultrasonic mist generator, obtaining promising results. However, the mist generator's inability to control droplet distribution presents limitations. To address this, we propose the utilisation of an ultrasonic spray atomiser, which overcomes these constraints. Our main objective is to develop a numerical model for this innovative system. Experimental data from a wind tunnel facility were employed to validate the model. A parametric analysis was conducted, considering key variables in the cooling process: injected water mass flow rate, cooled area, and atomiser power consumption. Based on these variables, an optimisation analysis was performed, revealing that the optimal operating ranges for overall performance are water-to-air mass flow ratios below $1.8 \cdot 10^{-3}$ for a relative humidity of 0.5, and below $8.1 \cdot 10^{-4}$ for 0.7. Within these conditions, water spray is more evenly distributed throughout the control section, facilitating a homogeneous and efficient evaporative cooling process. The maximum evaporative coefficient of performance achieved across all simulations was 30.49. That is, this novel equipment surpasses the limitations of previous systems and its performance.

1. Introduction

The Energy Efficiency First principle of the European Union requires that energy efficiency measures that are cost-effective be given the highest priority in shaping energy policy and making investment decisions. This comprehensive guiding principle can work in conjunction with other EU goals, particularly those related to sustainability, achieving climate neutrality, and promoting green growth. Essentially, the principle seeks to encourage the implementation of energy-efficient measures in all energy-related decisions, in order to achieve sustainable and environmentally conscious development. Buildings located in the European Union collectively account for 40% of our total energy consumption and 36% of the greenhouse gas emissions generated from activities such as construction, usage, renovation, and demolition. Enhancing the energy efficiency of these buildings is crucial in attaining the lofty objective of carbon-neutrality by the year 2050, as stated in the European Green Deal.

The application of evaporative pre-cooling techniques to the condenser of a refrigeration system represents a highly effective and readily applicable means of enhancing the efficiency of air conditioning systems in domestic and commercial settings globally, particularly in hot and arid climates. These techniques facilitate a significant reduction in energy consumption and demand peaks by introducing a small volume of water for a limited duration to cool the incoming air. Direct evaporative pre-cooling methods comprise wet media cooling and spray cooling.

Numerous studies in the literature have investigated the use of wetted media for pre-cooling air in various applications [1–3]. In air-conditioning applications, Martínez et al. [4] examined the impact of evaporative pad thickness on the energy consumption of a split-type air conditioner. Experimental results demonstrated that using a 100 mm pad thickness achieved a 10.6% improvement in the overall coefficient of performance (COP). Similarly, Ibrahim et al. [5] suggested the use of condensate to pre-cool the condenser air in a split-type air-conditioner, which led to a COP increase of 21.4% and an enhanced cooling capacity due to a temperature reduction of approximately 4 °C in the entering air. However, one of the main drawbacks of pre-cooling systems based on evaporative pads is the additional pressure drop generated in the condenser air stream, even when the pre-cooling is not active. Kumar et al. [6] evaluated a humidifier consisting of three cylindrical packings arranged in series, operating in rotary motion. It is observed that using the evaporative cooler consumes 42% less energy compared to the conventional air conditioning system.

Spray cooling is a widely researched technique for various applications, as evidenced by numerous papers in the literature [7–9]. Tissot et al. [10] employed an Eulerian–Lagrangian model to investigate

* Corresponding author.
E-mail address: j.ruiz@umh.es (J. Ruiz).

https://doi.org/10.1016/j.applthermaleng.2023.121455
Received 31 March 2023; Received in revised form 1 August 2023; Accepted 29 August 2023
Available online 4 September 2023

Nomenclature

A_T^x	percentage area for temperature T, at section x (–)
b	domain width (m)
C_D	drag coefficient (–)
d_d	droplet diameter (m)
F_c	safety factor numerical value in the GCI analysis ($F_c = 3$) (–)
g	gravitational constant (m s^{-2})
h	domain height (m)
h_C	heat transfer coefficient (W m^{-2} K^{-1})
h_D	mass transfer coefficient (kg m^{-2} s^{-1})
h_{fg}	enthalpy of vaporisation (J kg^{-1})
L	domain length (m)
l	distance between inlet sections (m)
L_w	wet length (m)
M	cumulative mass fraction (–)
m	mass (kg)
$\dot{m}_a$	air mass flow rate at the inlet section of the domain (kg s^{-1})
$\dot{m}_w$	mass flow rate of water spray (kg$_w$ s^{-1})
Nu	Nusselt number (–)
Δp	pressure loss (Pa)
p	pressure (Pa)
Pr	Prandtl number (–)
$\dot{Q}_{\text{cooling}}$	cooling capacity (W)
r	grid refinement ratio in the GCI analysis (–)
Re	Reynolds number (–)
s	order of convergence in the GCI analysis ($s = 2$) (–)
Sc	Schmidt number (–)
Sh	Sherwood number (–)
T	dry temperature (°C)
T_w	temperature of the water in the tank (°C)
T_{wb}	wet bulb temperature (°C)
$\bar{T}^x$	mean temperature calculated at section x (°C)
v_a	average air flow velocity in the wind tunnel (m s^{-1})
v_i	average air flow velocity in the spray discharge section (m s^{-1})
$\dot{W}_{\text{fan}}$	power absorbed by the fan (W)
$\dot{W}_{\text{pump}}$	power absorbed by the pump (W)
$\dot{W}_{\text{ultrasound}}$	power absorbed ultrasonic spray atomiser (W)
y	molar concentration (mol m^{-3})

Greek symbols

ε	relative error of the solutions in the GCI analysis (–)
μ	dynamic viscosity (kg m^{-1} s^{-1})
η_f	fan efficiency (–)
$\bar{\eta}^x$	evaporative cooling efficiency calculated at section x (–)
ϕ	relative humidity (–)
Re	Reynolds number (–)
ρ	density (kg m^{-3})
τ	stress tensor (kg m^{-3})

Subscripts

a	air
d	droplet
∞	ambient conditions
ma	moist air
w	evaporated water

Abbreviations

CFD	Computational Fluid Dynamics
COP	Coefficient of performance
GCI	Grid Convergence Index
HVAC	Heating, Ventilation and Air-Conditioning
MG	Mist Generator
SA	Spray Atomisers

droplet motion in an air flow, analysing droplet evaporation under different loadings, spray characteristics, and injection solutions in a small channel related to a real condenser. They concluded that an optimal cooling compromise requires balancing water droplet size and injection area. Raoult et al. [11] developed a CFD water spray model and investigated key physical parameters in evaporative cooling. They concluded that the Eulerian model is both simple and accurate, making it suitable for studying water spray evaporative cooling upstream of a heat exchanger.

Hou et al. [12] simulated the features of multi-nozzle arrangements for spray cooling, examining the effects of nozzle inlet pressure, mass flux, nozzle-to-surface distance, and nozzle numbers on droplet Sauter Mean Diameter (SMD or d_{32}). Sadafi et al. [9] demonstrated the potential of using saline water for pre-cooling inlet air to a heat exchanger, developing a CFD model to predict the wet length of saline water droplets in spray cooling under different ambient conditions and spray characteristics. They validated their model with their experimental data conducted in a wind tunnel, and presented a dimensionless correlation for wet length in horizontal flow. Kim et al. [13] numerically simulated a ultrasonic gas atomiser. They decided generation position and operating conditions of ultrasound atomiser. Zhang et al. (2020) performed a CFD study on a two-nozzle spray cooling system under different conditions. They validated the model for single droplet evaporation with a maximum relative error below 8%. The use of a single sprayer showed temperature deviations of 4.1% for dry bulb and 3.9% for wet bulb temperatures.

In recent years, there has been an increasing interest in exploring the use of ultrasonic energy to enhance various processes and improve system efficiency. Yao [14] conducted a literature review to address the potential applications of ultrasound as a new technology in Heating, Ventilation and Air-Conditioning (HVAC). The author concluded that ultrasound could produce various effects that could be useful in applications involving heat or mass transport by decreasing both the external and internal resistance to transport. Despite this potential, evaporative cooling has not received much attention in the context of ultrasound applications as pointed out by Yao et al. [15] in their state-of-the-art review on high-intensity ultrasound and its applications, where they did not specifically mention it as an application.

Up to the knowledge of the authors, the study conducted by Martinez et al. [16] was the first attempt to apply ultrasonic techniques (mist generator) to pre-cool the air entering the condenser in an air conditioning application. The authors experimentally analysed the performance of an ultrasonic mist generation system. Its thermal performance and its water mist production capacity were assessed in terms of the mass flow rate of atomised water and size distribution of the droplets generated. The same research group, in Ruiz et al. [17], developed and reported a CFD model of the ultrasonic mist generator tested in [16].

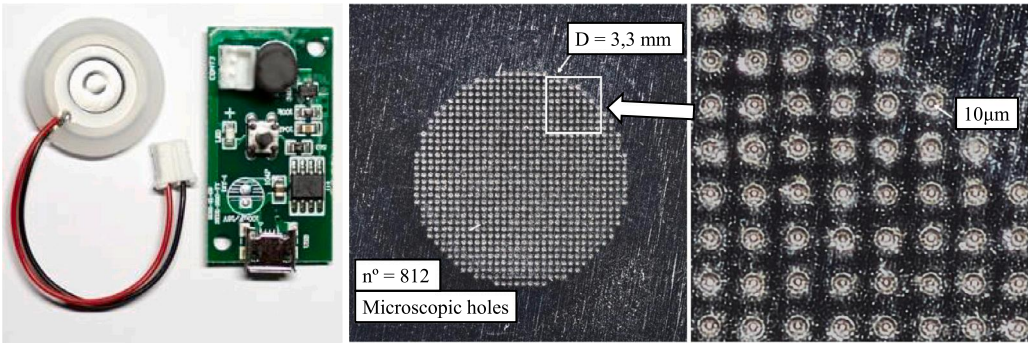

(a) Ultrasonic spray atomisers. (b) Microscopic image of the water outlet holes.

Fig. 1. (a) Used ultrasonic spray atomisers and an oscillator circuit PCB. (b) Microscopic image of the water outlet holes in the spray atomisers used.

The authors conducted a parametric analysis including some physical variables involved in the cooling process, and, finally, carried out an optimisation process regarding the overall cooling performance of the ultrasonic generator.

The literature review carried out has highlighted that ultrasonic devices constitute a promising approach to improve the performance of air conditioning systems via the pre-cooling of the inlet air to the condenser. However, little attention has been paid to them. Among the major drawbacks of ultrasonic mist generation systems, the wet length (i.e. travelling distance of liquid droplets without evaporating) and the equipment power consumption can be pointed out. This fact constituted the main motivation of this work.

The ultrasonic mist generator is composed of a compact mist maker device with 10 ultrasonic transducers, which is submerged in a water tank. These transducers have the ability to convert high-frequency electronic signals into mechanical oscillations with a high frequency on the disc. As the ceramic disc moves, the water imitates its motion and tries to match the high-frequency oscillations. This leads to the separation of the water from the disc during the negative oscillations, creating a temporary void where cavitation occurs and the water undergoes a transformation into steam. Subsequently, during the positive oscillation phase, the steam water is forcefully propelled upward by the high pressure wave, traversing the water surface. In this adiabatic process, a mist water is generated (droplets with diameters ranging from a few tens of microns). However, due to its mode of operation and being a compact device, the mist generator forms a singular stream of mist water over which there is little control.

In order to overcome the mist generator limitations mentioned above, an ultrasonic spray atomiser is proposed in this research. Compared to an ultrasonic mist generator, an ultrasonic spray atomiser presents several advantages, such as lower power consumption, lower cost, and a more homogeneous droplet distribution that favours the evaporation, improving the cooling efficiency and reducing the wet length. This is because, although the operation is comparable, in this case of the ultrasonic spray atomiser system, each atomiser generates a different current. This enables a more straightforward regulation of the plume's distribution that they produce.

In this sense, the main objective of this study was to develop a numerical model of an ultrasonic spray atomisers system. No studies on this nature have been previously reported in the literature, highlighting the novelty of the research presented in this paper. The CFD model was validated with experimental data and was used to assess the performance of the system and to optimise the arrangement of the atomisers in order to maximise the evaporative efficiency and to reduce the wet length with the minimum power consumption.

The structure of this paper can be outlined as follows. Section 2 describes the experimental setup and provides an overview of the CFD model. Section 3 presents the results obtained from the CFD model, including the parametric analysis and optimisation. The key findings of this study are summarised in Section 4.

Table 1
Spray atomiser technical specifications.

Disc diameter	15.5 mm
Ceramic core diameter	8.5 mm
Porous membrane diameter	3.3 mm
Microscopic Holes Diameter	10 μm
Input voltage	DC 5 V
Power	1.3 W
Resonance frequency	108 kHz
Mass flow rate	$1.95 \cdot 10^{-5}$ kg s^{-1}
Exit speed of the drops	2.5 m s^{-1}

2. Materials and methods

2.1. Experimental test facility

A set of experimental tests were carried out to obtain the key parameters to validate the CFD model. The test facility mainly consists of two components: an ultrasonic system based on spray atomisers and a wind tunnel.

The ultrasonic spray atomiser system used in the experiments is shown Fig. 1(a). This device utilise the power of ultrasonic vibrations to atomise liquids into fine particles or droplets, generating a mist or spray. It consists of a porous metallic membrane surrounded by a piezoelectric ceramic disc, and an oscillator circuit PCB that generates a pulse signal at a frequency of 108 kHz for the spray atomiser. When the current is supplied, the ultrasonic transducer convert electrical energy into mechanical vibrations and the piezoelectric initiates an expansion/contraction cycle. These high-frequency vibrations create pressure waves within the liquid, causing it to break up into tiny droplets that are subsequently dispersed as a fine spray. The water pass through the microscopic holes (around 10 μm, Fig. 1(b)), and pushes the drops forming a column of water spray. The mass flow rate is approximately $1.95 \cdot 10^{-5}$ kg s^{-1}. This component is characterised by having a low cost and consumption (1.3 W). Table 1 shows the operating conditions and technical specifications of a spray atomiser.

Several atomisers (25) were assembled in a manifold manufactured in flexible silicone pipes. An ABS plastic body was used to connect the atomisers with the pipes. A low-flow pump (RS PRO 20) was used for the recirculation of the water (maximum flow rate of 650 ml min^{-1} and a consumption of 5 W). Fig. 2 shows a schematic representation of the hydraulic system used in the experiments with 5 × 5 atomisers (rows × columns) and its experimental setup in the wind tunnel.

To carry out the experimental tests of ultrasonic evaporative cooling, the open-circuit subsonic wind tunnel shown in Fig. 3 was used. To ensure stable and uniform velocity profiles of the airflow, a nozzle was used along the honeycomb baffle (anti-turbulence screen), which was adapted for the tunnel entrance (leftmost part). This nozzle has dimensions of 1.2×1.7 m^2 (cross-sectional) and a length of 1.55 m. The

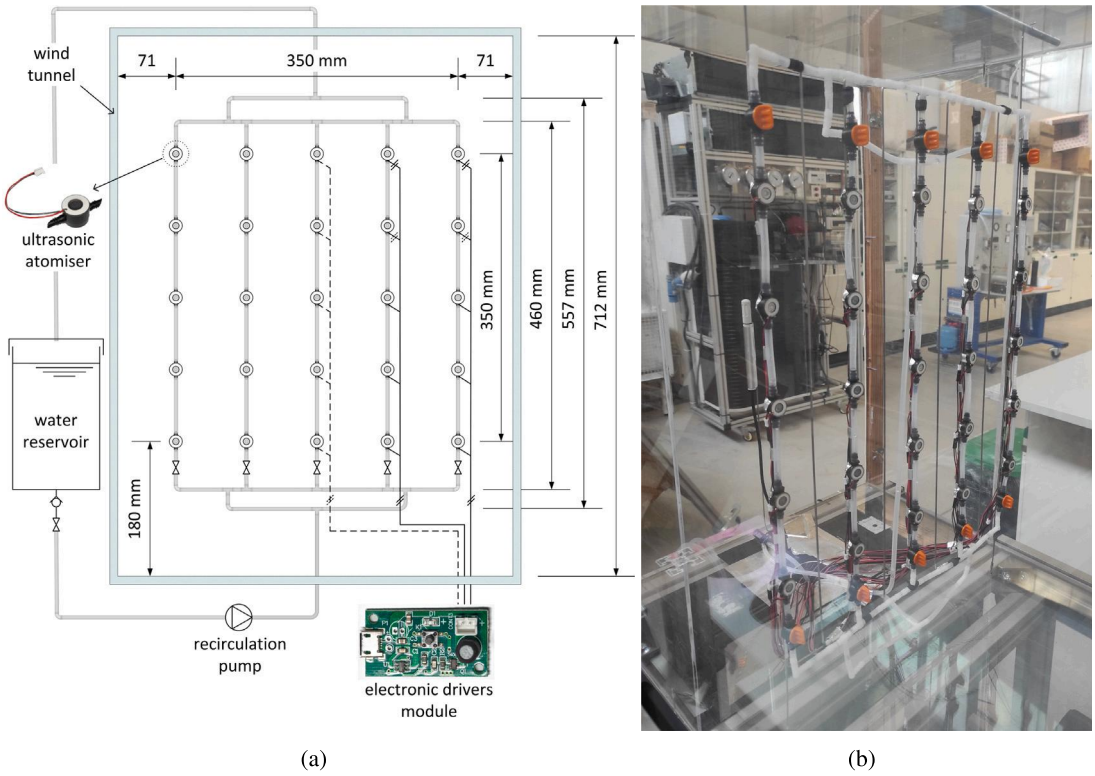

Fig. 2. Scheme of the distribution of the spray atomisers in the form of a 5 × 5 manifold and its experimental setup in the wind tunnel.

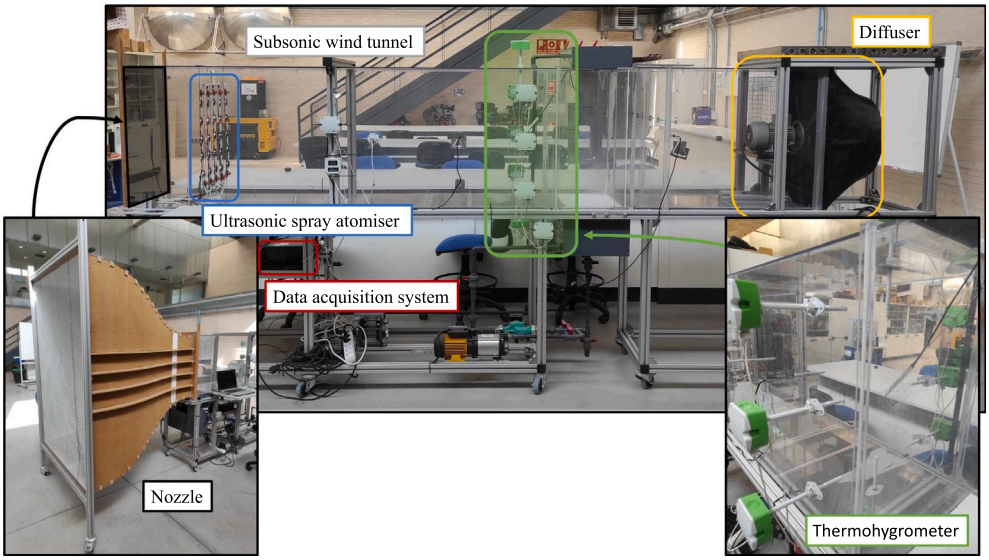

Fig. 3. Subsonic wind tunnel facility in which the experimental tests are carried out.

test section of the wind tunnel has a cross section of 0.492×0.712 m^2 and a length of 5.3 m. A axial fan of 0.55-kW was used to create the air flow inside the tunnel, which is located at the tunnel exit. This is connected with a variable-frequency drive that allows different air flows to be configured (from 0–3 m s^{-1}). The maximum volumetric air flow rate allowed by the fan is 3783 m^3 h^{-1}. A detailed description of the wind tunnel can be found in [18–20].

2.2. Experimental procedure

As mentioned in Section 2.1, in this work several experimental tests were carried out to validate the developed numerical model. Table 2 shows the main magnitudes registered by the sensors installed in the wind tunnel. These sensors were distributed throughout the test rig. Fig. 4 depicts an schematic arrangement of the location of all sensors.

To determine the injected mass flowrate of water, a gravimetric method was used. It consists of measuring the weight of the water used by the spray atomisers in a certain time by means of a high-precision scale. This was done by measuring the weight of the make-up water reservoir.

A thermohygrometer was installed at the inlet of the wind tunnel to measure the inlet air dry-bulb temperature (ambient, T_∞) and the relative humidity (ϕ_∞). Additionally, three more thermohygrometers

Table 2
Summary of the magnitudes registered during the experimental tests.

Test run	Configuration	v_a (m s^{-1})	$\dot{m}_w$ (kg s^{-1})	T_∞ (°C)	ϕ_∞ (%)	T_1 (°C)	ϕ_1 (%)	T_2 (°C)	ϕ_2 (%)	T_{ms} (°C)	ϕ_{ms} (%)	T_3 (°C)	ϕ_3 (%)
1	5 × 1	0.5	$9.77{\cdot}10^{-5}$	29.34	54.68	27.27	65.05	28.61	55.03	28.05	60.39	28.46	56.21
2	5 × 1	1.0	$9.77{\cdot}10^{-5}$	28.84	47.27	27.93	50.45	28.00	47.41	28.30	48.69	27.89	48.93
3	5 × 1	1.5	$9.77{\cdot}10^{-5}$	28.05	60.14	27.12	65.77	27.11	62.36	27.58	62.11	27.02	64.29
4	5 × 1	2.0	$9.77{\cdot}10^{-5}$	28.80	57.03	28.04	61.03	27.98	58.21	28.38	58.37	27.88	59.51
5	5 × 3	0.5	$2.93{\cdot}10^{-4}$	29.46	54.76	25.24	79.44	25.32	74.96	26.25	73.22	24.86	81.20
6	5 × 3	1.0	$2.93{\cdot}10^{-4}$	28.72	49.35	26.90	57.65	26.76	55.35	27.15	56.36	26.51	57.32
7	5 × 3	1.5	$2.93{\cdot}10^{-4}$	29.21	53.92	27.53	62.21	27.60	58.46	28.05	58.60	27.30	60.78
8	5 × 3	2.0	$2.93{\cdot}10^{-4}$	29.55	53.04	28.28	58.83	28.33	55.72	28.60	56.70	27.92	58.74
9	5 × 5	0.5	$4.88{\cdot}10^{-4}$	29.51	45.39	22.67	85.34	23.03	78.04	24.29	73.93	24.14	75.01
10	5 × 5	1.0	$4.88{\cdot}10^{-4}$	30.89	36.32	26.26	55.44	26.17	52.45	28.48	44.14	26.76	50.44
11	5 × 5	1.5	$4.88{\cdot}10^{-4}$	29.38	40.37	26.24	53.48	26.18	50.94	27.66	45.98	26.46	52.04
12	5 × 5	2.0	$4.88{\cdot}10^{-4}$	29.23	40.73	26.75	50.58	26.73	47.71	27.93	44.68	26.84	50.17

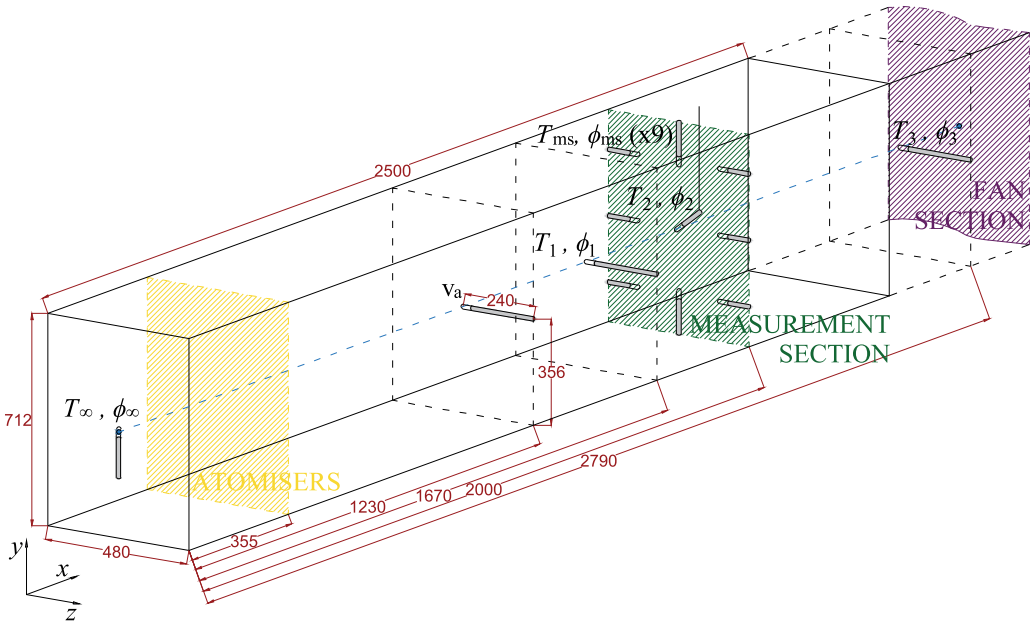

Fig. 4. Schematic arrangement of the test section, spray atomisers system and measurement devices, with dimensions in mm.

were used to register the distribution of relative humidity and temperature in the longitudinal section (T_1, T_2, T_3, ϕ_1, ϕ_2, and ϕ_3), which were located downstream of the spray water discharge section in the centre of the tunnel at 1315, 1645 and 2435 mm, respectively. On the other hand, an array of nine thermo-hygrometers was used to register the temperature and relative humidity distribution in the transverse section. T_{ms} and ϕ_{ms} refer to the mean temperature and relative humidity of these 9 measurements. The temperature and humidity registered by the sensor placed at the centre, matches with T_2 and ϕ_2. Finally, a hot-wire anemometer, placed 875 mm downstream of the section where the ultrasonic spray atomisers are located, was used to measure the averaged air flow velocity in the wind tunnel, v_a. As discussed in [18], the use of the nozzle ensures that the velocity profile in the test section of the wind tunnel is uniform. In addition, the installation was calibrated to obtain, with an experimental correlation, the mean air velocity from the local velocity in its centre. So, this measurement is enough to know the mean velocity and, hence, the volumetric flow.

Table 3 shows the technical specifications and accuracy of the test bench probes used in both the wind tunnel calibration tests and during the experimental characterisation tests of the ultrasonic spray atomiser. All measurements were recorded with a Keysight DAQ970A data acquisition unit incorporating two Keysight DAQM901A 20-channel multiplexer modules.

In order to determine the size and velocity of the injected drops, a high-resolution direct photography technique (pixel shift) was employed, as described by Ramisetty [21]. The droplets were ejected through the discharge tube of the test rig and photographed using a Pentax K-1 camera, with a maximum shutter speed of 1/8000 s and a Tamron SP AF 90 mm F2.8 Di Macro 1:1 lens attached. To achieve higher lens magnification, an 18 cm extension tube was used. To freeze the droplet movement as they were ejected, a Pentax AF-360 FGZ auto flash unit was used in TTL flash mode, with a 1/2 peak duration time of approximately 1/20000 s. The flash was arranged on the opposite side of the camera position, and a remote trigger was used to take the photographs while keeping the water mist flowing between the two devices. In order to simplify the photographic analysis, the light from the flash was channelled through a 3 mm slit made of a plastic sheet, creating a narrow illumination plane to isolate the droplets. Only the droplets passing through that illumination plane were captured by the camera. An f-stop number of f/2.8 was used to boost the isolation of the droplets captured in the shots, producing a pronounced blurring of out-of-focus droplets, which were not counted in the subsequent photographic analysis. The photographs had a native resolution of 7360 × 4912 pixels and were processed with a graphic editor to increase contrast and acutance. The uncertainty of the measurement method was estimated by considering a variation of ±1 pixel in the measurement of the droplet diameter using digital image processing, as shown in Fig. 5.

2.3. Physical model

The physical domain used in the simulations reproduces a part of the wind tunnel where these tests have been carried out. The domain

Table 3
Specifications and characteristics of the test bench probes used during the experimental tests.

Measurement	Measuring device	Brand	Model	Measuring range	Output signal	Accuracy
Air temperature	Thermohygrometer	E+E Elektronik	EE210-HT6xPBFxB	−20 to 80 °C	4–20 mA	±0.2 °C
Air humidity	Thermohygrometer	E+E Elektronik	EE210-HT6xPBFxB	0%–100%	4–20 mA	± (1.3+0.3% RD)%
Air temperature	Thermohygrometer	E+E Elektronik	EE210-HT6xPCxx	−20 to 80 °C	4–20 mA	±0.2 °C
Air humidity	Thermohygrometer	E+E Elektronik	EE210-HT6xPCxx	0%–100%	4–20 mA	± 2.5%
Air flow velocity	Anemometer	E+E Elektronik	EE65-VCD02	0–20 m/s	4–20 mA	± (0.2 m/s + 3% RD)
Air flow rate	Flow hood balometer	Testo	0563 4200	40–4000 m^3/h	USB port	± (12 m^3/h + 3% RD)
Power consump.	Power quality analyser	Chauvin Arnoux	8334		USB port	± 1% RD
Water temperature	RTD-Pt100	Desin	ST-FFH PT100	−200 to 600 °C	4-wires	±0.05 °C
Water weight	Benchtop scale	PCE Instruments	PCE-TB 3	0–3 kg	4–20 mA	± 0.1 g

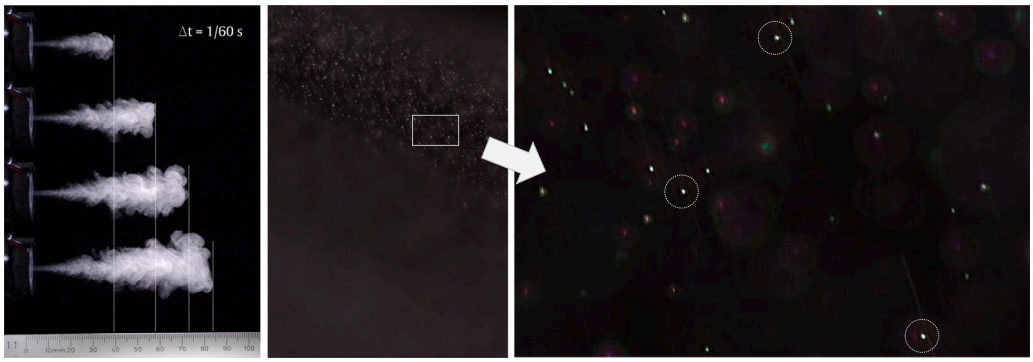

(a) (b)

Fig. 5. Experimental test carried out to define: (a) velocity, and (b) size of the injected drops.

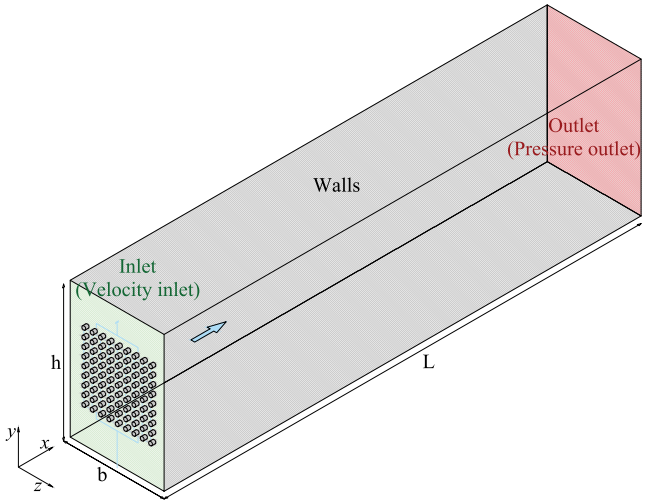

Fig. 6. Domain and boundary conditions used in the simulations.

is 2.5 m long, 0.712 m high and 0.492 m wide ($L \times h \times b$, Fig. 6). The water spray injections are set out at the air inlet section in parallel with the air flow. It corresponds with the position where the spray atomisers are installed. These are included evenly distributed in a square of 0.35×0.35 m^2 in the centre of the inlet section.

2.4. Mathematical method (governing equations)

In evaporative cooling processes, there is mass, heat, and momentum transfer between the water droplets and the moist, unsaturated air stream. It is for this reason that, to study these processes, the conservation principles of momentum, mass, energy and species must be taken into account. This multiphase flow can be described by the equations governing the continuous phase (moist air in the wind tunnel) and the equations that govern the discrete phase (water droplets generated by the ultrasonic generator). In this work, the Eulerian–Lagrangian approach has been used.

2.4.1. Continuous phase (moist air)

This section summarises the main considerations that have been taken into account to model the continuous phase. As for the air flow, it has been considered steady, turbulent and incompressible. The Reynolds-Averaged Navier–Stokes (RANS) equations have been used along the standard $\kappa - \epsilon$ turbulence model. Although most turbulence models perform similarly [8], some authors have reported that in spray cooling applications, the standard $\kappa - \epsilon$ turbulence model is able to accurately predict droplet evaporation and flow field [7,22–24].

The governing equations for the continuous phase (conservation of mass, momentum, energy and diffusion of species) are shown in Eqs. (1)–(5). In order to take into account the influence that the water droplets have on the air flow, the source terms of mass, momentum and energy have been introduced into the air-side governing equations.

$$\frac{\partial\left(\rho v_i\right)}{\partial x_j} = S_m \tag{1}$$

$$\frac{\partial\left(\rho v_i v_j\right)}{\partial x_j} = -\frac{\partial p}{\partial x_i} + \frac{\partial \tau_{ij}}{\partial x_j} + \rho g_i + S_{mo} \tag{2}$$

$$\rho v_i \frac{\partial e}{\partial x_j} = -p\frac{\partial v_i}{\partial x_j} + \frac{\partial}{\partial x_j}\left(k\frac{\partial T}{\partial x_j}\right) + \frac{\partial}{\partial x_j}\left(\sum_{i'=1}^{n} h_{i'} J_{i'}\right) + \phi_v + S_e \tag{3}$$

$$\rho v_i \frac{\partial m_j}{\partial x_j} = -\frac{\partial J_{i',i}}{\partial x_j} + S_m \tag{4}$$

$$J_{i',i} = -\rho D_{f_{i',m}} \frac{\partial m_j}{\partial x_j} \tag{5}$$

Here, the momentum, mass and energy source terms introduced by the water droplets are S_m, S_{mo} and S_e, respectively. The diffusion flux of the species i' is represented by $J_{i',i}$.

2.4.2. Discrete phase

A Lagrangian model has been used to model the equations that describe the behaviour of spherical water droplets. The force balance

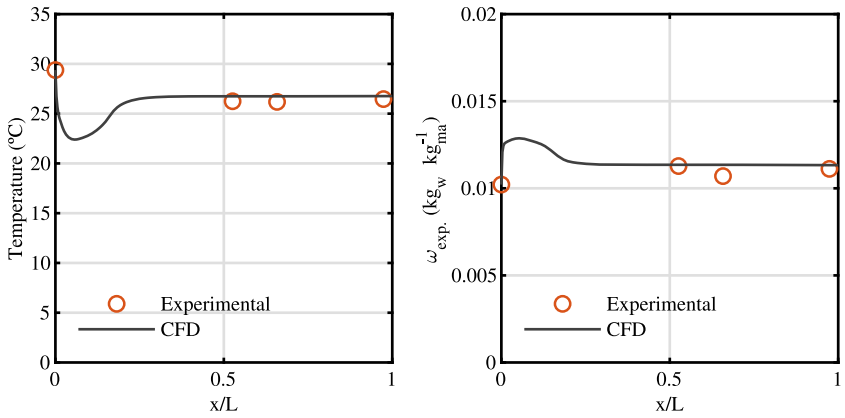

Fig. 7. Comparison between experimental and predicted results (temperature and water mass fraction) at the longitudinal section for the test run 11 in Table 2.

on the droplet (Newton's second law) has been integrated to obtain the trajectory of the particles, Eqs. (6)–(7).

$$\frac{dv_d}{dt} = \frac{18\mu}{\rho_d d_d^2}\frac{C_D \mathrm{Re}}{24}\left(v - v_d\right) + g\frac{\rho_d - \rho}{\rho_d} \tag{6}$$

$$\frac{dr_d}{dt} = v_d \tag{7}$$

The method described in [25] has been used to calculate the drag coefficient (C_D) that appears in the drag per unit droplet mass term. Owing to the temperature and vapour concentration differences, heat and mass transfer between the unsaturated air and the water droplets occur. If the radiation effect is neglected, the energy conservation equation for a droplet can be expressed as in Eq. (8), where the temperature change in the droplet is related to the latent and convective heat transfer between the continuous phase and the droplet.

$$m_d c_p \frac{dT_d}{dt} = h_C A_d \left(T - T_d\right) + \frac{dm_d}{dt} h_{fg} \tag{8}$$

The change in the rate of evaporation of the water is expressed by,

$$\frac{dm_d}{dt} = h_D A_d M \left(y_s - y\right) = h_D A_d \left(\rho_s - \rho\right) \tag{9}$$

The Nusselt and Sherwood numerical correlations described by [26,27] have been used to calculate the mass and convective transfer coefficients (h_D, h_C),

$$\mathrm{Nu} = \frac{h_C d_d}{k} = 2 + 0.6\,\mathrm{Re}_d^{1/2}\,\mathrm{Pr}^{1/2} \tag{10}$$

$$\mathrm{Sh} = \frac{h_D d_d}{D_f} = 2 + 0.6\,\mathrm{Re}_d^{1/2}\,\mathrm{Sc}^{1/2} \tag{11}$$

2.5. Numerical method

Fig. 6 also includes the boundary conditions used in the simulations. The air inlet section is located at the left side of the tunnel and the air velocity was fixed as in the experiments. The dispersion of the droplets due to turbulence was modelled using the stochastic tracking model referred to as Discrete Random Walk in ANSYS FLUENT. By calculating the trajectory of a representative number of particles (tries), the model is capable of simulating the random effects of turbulence and predicting the particle dispersion. Five tries were used in the simulations, meaning that the number of particles set out was multiplied by 5. According to Ruiz et al. [28], a turbulence intensity of 5% was assumed for the inflows. The incoming spray water was adjusted to match the experimental observations. On the other hand, the temperature of the drops was set equal to the inlet air temperature used in each simulation. In the case of the pressure at the outlet section, it was assumed to be equal to the ambient pressure. For the tunnel walls, wall boundary condition without slip and with zero heat flux was chosen. It was established that if the drops reached the walls or the tunnel exit, they left the computational domain (escape boundary condition), [7]. For the droplet size distribution, 10 μm was considered. It corresponds to the size of the droplets generated by the spray atomiser (Fig. 5(b)).

The commercial code ANSYS FLUENT (version 21 R1) [29] was utilised to numerically solve the governing equations. To ensure the accuracy of the numerical outcomes, a grid independence investigation was carried out using the Grid Convergence Index (GCI) method, as proposed by [30]. The GCI serves as a metric to quantify the discrepancy between the computed and asymptotic numerical values. In simpler terms, it provides an error band indicating the deviation of the solution from the asymptotic value. Mathematically, the GCI can be computed as follows,

$$\mathrm{GCI} = \frac{F_c|\varepsilon|}{r^s - 1} \tag{12}$$

To check the independence of the mesh on the results, several grids of different sizes were generated using ANSYS MESHING. The GCI was calculated for the anticipated temperature and absolute humidity values at the measurement plane. The highest GCI observed in the fine-grid solution for these parameters is 0.04%. This GCI value implies an insignificant impact of the grid resolution on the results. The mesh that reported physical and stable results with the least number of elements was chosen. An structured grid with 2,087,910 cells was selected. To solve the coupling between the momentum and continuity equations through pressure, the SIMPLE algorithm was used. The calculations were conducted using second order discretisation. The convergence criterion was $|\varphi(i+1) - \varphi(i)|/\varphi(i) < 10^{-4}$, where i represents the iteration number and φ can indicate any of the dependent variables.

3. Results and discussion

3.1. Model validation

Six out of twelve cases were used for validation purposes. Two variables were modified in the simulations: the number and distribution of the atomisers, and the air inlet velocity. As previously explained, the configuration column in Table 2 ($r \times c$), corresponds to the number of rows and columns activated during the experiments. All the cases with a configuration of 5×5, as well as the 5×1 and 5×3 with $v_a = 1.5$ m s^{-1} were simulated and compared to the experiments (test runs 3, 7, 9, 10, 11 and 12 in Table 2).

Taking as an example the simulation corresponding to test run number 11 in Table 2, Figs. 7 and 8 show the comparison in terms of temperature and water mass fraction between the experimental results observed at the specific locations where the sensors are placed and the evolution of the plume predicted by the numerical model throughout the entire section. Fig. 7 depicts the longitudinal evolution (3 points at the wind tunnel centreline) and Fig. 8 shows the measurements at

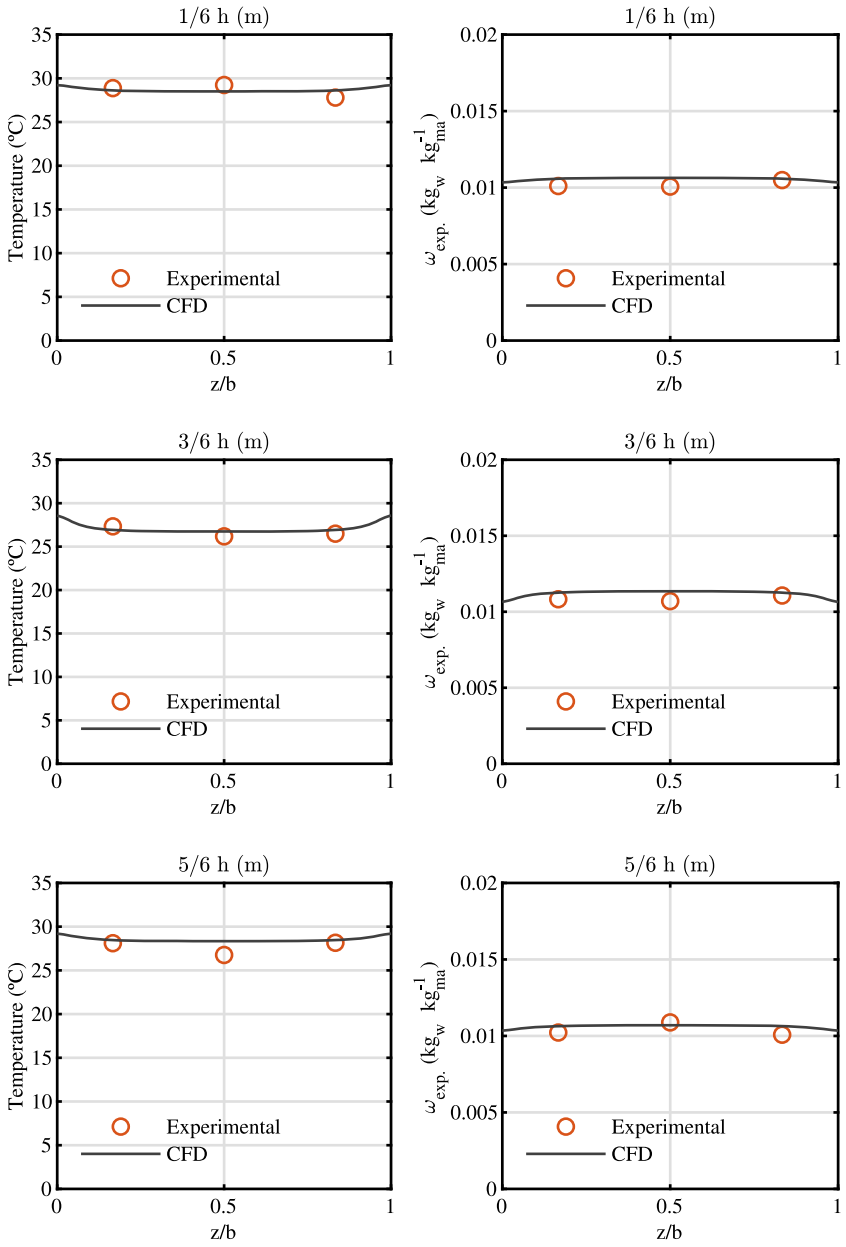

Fig. 8. Comparison between experimental and predicted results (temperature and water mass fraction) at the cross-sectional area where the sensors are placed for the test run 11 in Table 2.

the cross-sectional area where the sensors array is placed (green-shaded plane in Fig. 4). As it can be seen, an excellent agreement is observed between predicted and experimental results.

Fig. 9 shows the comparison between CFD and experimental results for all the simulations and the eleven measuring locations. Fig. 9(a) depicts the temperature comparison. It can be stated that, on average, the difference is ±0.81 °C, which corresponds to a 3.1% deviation. The one case deviating more than 4 °C corresponds to $v_a = 0.5$ m s^{-1} and this variation is justified by the lack of stationarity conditions observed during the experimental test. Fig. 9(b) shows the mass fraction comparison. Again, it can said that the predictions are reliable since most of the point cloud is below ±1.0 g_w kg_{ma}^{-1}. The average difference is ±0.5 g_w kg_{ma}^{-1} which translates into 4.2% difference. Therefore, in light of these results, the model can be considered validated, since, in all the compared cases, the results are below the 5% on average.

3.2. Parametric analysis

Once the model was validated, a parametric study was carried out to assess the performance of the new evaporative system of ultrasonic spray atomisers operating in different conditions. Thirty-one cases were simulated in the parametric study. The variables and levels considered in the simulations are shown in Table 4, and cover the number and arrangement of the atomisers, the average air flow axial velocity, and the environmental conditions such as temperature and air humidity. These variables were chosen due to the fact that it was difficult to study them independently with an experimental approach. Two levels for the axial velocity were considered: 1.0 and 1.5 m s^{-1}. This is justified because the operating conditions of low-to-medium power range air-cooled condensers are usually between 0.5 to 2.5 m s^{-1}, and most commonly 1 to 1.5 m s^{-1}. Two additional levels of temperature (25

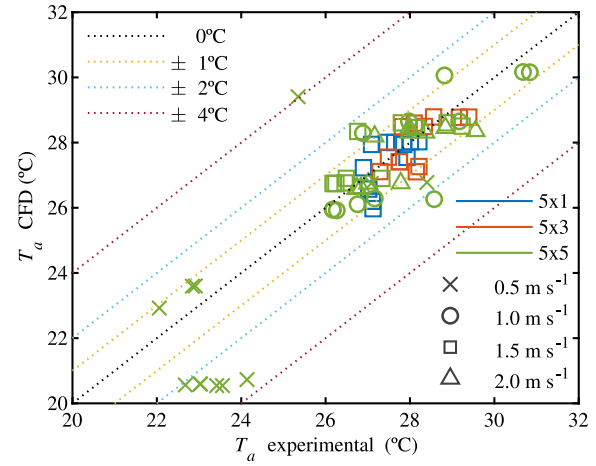

(a) Dry-bulb temperature.

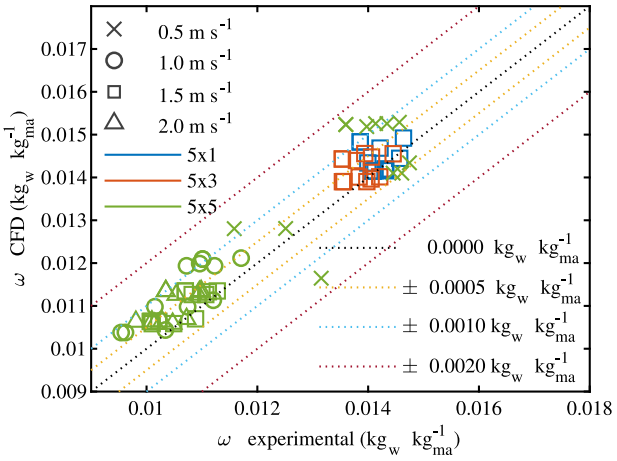

(b) Water mass fraction.

Fig. 9. (a) Temperature and (b) water mass fraction comparison between CFD and experimental results for tests 3, 7, 9, 10, 11 and 12 in Table 2.

and 30 °C) and air relative humidity (50 and 70%) were set. Finally, different atomiser arrangements were studied. The number of atomisers ranged from 16 to 64 (4 × 4, 8 × 8) for the different simulation sets studied. The atomisers were evenly arranged in a 0.35×0.35 m^2 square in the centre of the inlet area, as explained in Section 2.1. The injected water mass flowrate by each atomiser is fixed, so the total amount of injected water is directly related to the number of atomisers included in the simulation. The rest of the variables involved in the parametric analysis were considered constant with values similar than the ones registered during the experimental tests ($T_w = T_\infty$ and $d_d = 10$ µm). Table 5 contains the information of the simulations conducted.

Fig. 10 shows, as an example, the temperature contours (Figs. 10(a) and 10(b)), humidity contours (Figs. 10(c) and 10(d)), and the evolution of the water droplets along the domain (Figs. 10(e) and 10(f)) for two simulations with $T_\infty = 25$ °C, $\phi_\infty = 0.5$, $v_a = 1.5$ m s^{-1}, and 25 and 49 atomisers, respectively (cases 16 and 18 in Table 5). As it can be seen, since the injections are uniformly distributed in the inlet section, the evolution of the temperature contours is also quite uniform throughout the entire domain and the exit section of the tunnel, once all the drops have evaporated. Therefore, for calculation purposes, from now on, the average temperature at the exit section of the tunnel, $\bar{T}^L$, is considered for discussion purposes.

Table 4
Variables and levels considered in the parametric study.

Distribution	N° atomisers	v_a (m s^{-1})	T_∞ (°C)	ϕ_∞ (–)
4 × 4, 5 × 5, 6 × 6	16, 25, 36	1.0	25	0.5
7 × 7, 8 × 8	49, 64	1.5	30	0.7

Table 5
Summary of the simulations conducted.

Case	Configuration	T_∞ (°C)	ϕ_∞ (%)	v_a (m s^{-1})	$\dot{m}_w$ (kg s^{-1})
1	4 × 4	25	50	1	$3.13 \cdot 10^{-4}$
2	5 × 5	25	50	1	$4.88 \cdot 10^{-4}$
3	6 × 6	25	50	1	$7.03 \cdot 10^{-4}$
4	7 × 7	25	50	1	$9.57 \cdot 10^{-4}$
5	4 × 4	25	70	1	$3.13 \cdot 10^{-4}$
6	5 × 5	25	70	1	$4.88 \cdot 10^{-4}$
7	6 × 6	25	70	1	$7.03 \cdot 10^{-4}$
8	4 × 4	30	50	1	$3.13 \cdot 10^{-4}$
9	5 × 5	30	50	1	$4.88 \cdot 10^{-4}$
10	6 × 6	30	50	1	$7.03 \cdot 10^{-4}$
11	7 × 7	30	50	1	$9.57 \cdot 10^{-4}$
12	4 × 4	30	70	1	$3.13 \cdot 10^{-4}$
13	5 × 5	30	70	1	$4.88 \cdot 10^{-4}$
14	6 × 6	30	70	1	$7.03 \cdot 10^{-4}$
15	4 × 4	25	50	1.5	$3.13 \cdot 10^{-4}$
16	5 × 5	25	50	1.5	$4.88 \cdot 10^{-4}$
17	6 × 6	25	50	1.5	$7.03 \cdot 10^{-4}$
18	7 × 7	25	50	1.5	$9.57 \cdot 10^{-4}$
19	8 × 8	25	50	1.5	$1.25 \cdot 10^{-3}$
20	4 × 4	25	70	1.5	$3.13 \cdot 10^{-4}$
21	5 × 5	25	70	1.5	$4.88 \cdot 10^{-4}$
22	6 × 6	25	70	1.5	$7.03 \cdot 10^{-4}$
23	4 × 4	30	50	1.5	$3.13 \cdot 10^{-4}$
24	5 × 5	30	50	1.5	$4.88 \cdot 10^{-4}$
25	6 × 6	30	50	1.5	$7.03 \cdot 10^{-4}$
26	7 × 7	30	50	1.5	$9.57 \cdot 10^{-4}$
27	8 × 8	30	50	1.5	$1.25 \cdot 10^{-3}$
28	4 × 4	30	70	1.5	$3.13 \cdot 10^{-4}$
29	5 × 5	30	70	1.5	$4.88 \cdot 10^{-4}$
30	6 × 6	30	70	1.5	$7.03 \cdot 10^{-4}$
31	7 × 7	30	70	1.5	$9.57 \cdot 10^{-4}$

3.2.1. Air temperature difference

Fig. 11 shows the temperature difference between the inlet and outlet air temperatures ($\Delta T = T_\infty - \bar{T}^L$) for all the simulations conducted. The general trend observed is that ΔT increases for increasing $\dot{m}_w/\dot{m}_a$ values. An increase in the water-to-air mass flow ratio ($\dot{m}_w/\dot{m}_a$) can be interpreted as, if for a fixed mass flow rate of air ($\dot{m}_a$), the amount of injected water ($\dot{m}_w$, number of atomisers) increases. If the air is not saturated, increasing $\dot{m}_w/\dot{m}_a$, increases the evaporation rate and reduces $\bar{T}^L$. This statement is valid until saturation is reached. In this case, an increase in $\dot{m}_w/\dot{m}_a$ does not result in an increase in the evaporation rate.

The influence of the ambient conditions (temperature and humidity) on the temperature difference (ΔT) is negligible with the exception of the cases with high humidity levels and high water-to-air mass flow ratios. This is better explained with the aid of Fig. 12, where the evolution of the air properties in the psychrometric chart is shown. The process studied corresponds to an isenthalpic evolution. For the same amount of air, an increase in the mass flow of water (increasing the number of atomisers) always translates into greater humidity ratio. This, in turn, translates into a lower final temperature, with the exception of the cases in which complete evaporation of the drops does not occur because saturation is reached. This justifies the asymptotic behaviour observed in Fig. 11 for high $\dot{m}_w/\dot{m}_a$ and ϕ_∞ levels. The fact that Fig. 12 does not show that the air reaches full saturation is due to the conditions represented are the average conditions of the outlet air. However, if Fig. 10(d) is observed, it can be seen that in the air plume, where the droplets are concentrated, the air is completely saturated. The largest ΔT is 4.82 °C and occurs for the case of 49 atomisers, $v_a = 1.0$ m s^{-1}, $T_\infty = 30$ °C and $\phi_\infty = 0.5$ (simulation 4, Table 5).

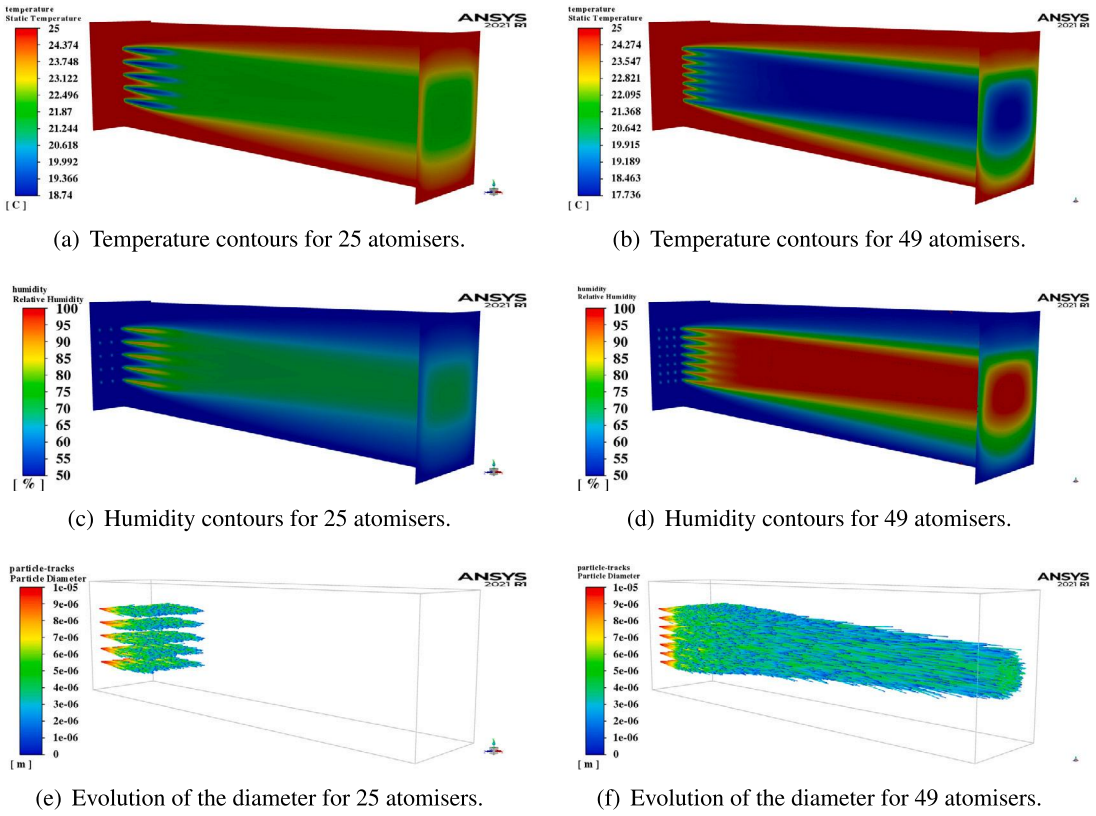

(a) Temperature contours for 25 atomisers. (b) Temperature contours for 49 atomisers.

(c) Humidity contours for 25 atomisers. (d) Humidity contours for 49 atomisers.

(e) Evolution of the diameter for 25 atomisers. (f) Evolution of the diameter for 49 atomisers.

Fig. 10. Contours in the axial mid plane and the outlet section of the domain and evolution of the diameter of the drops from when they leave the spray atomisers until they completely evaporate or leave the domain for the test 16 and 18 in Table 5.

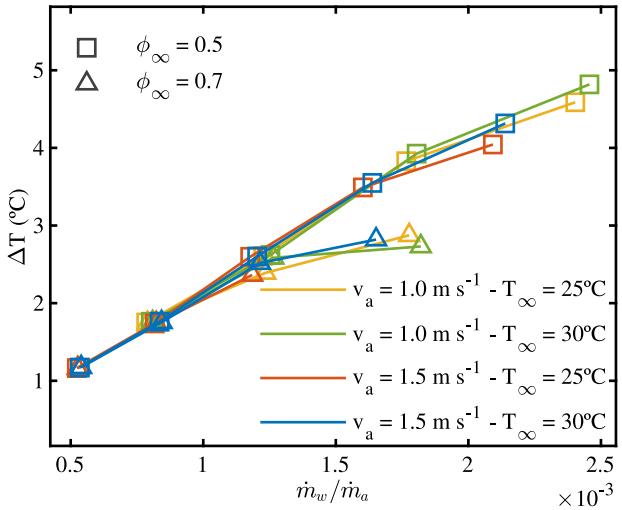

Fig. 11. Air temperature difference between inlet and outlet as a function of the water-to-air mass flow ratio for all simulations conducted.

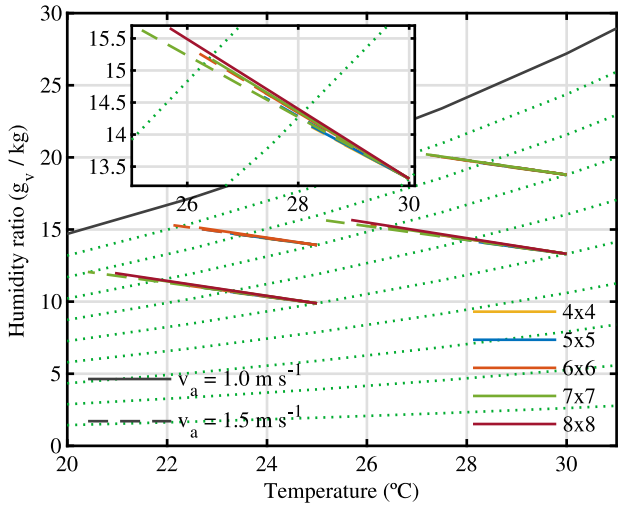

Fig. 12. Evolution of the properties of air in a psychrometric chart.

3.2.2. Evaporative cooling efficiency

The following section discusses the efficiency of evaporative cooling at a specific section, denoted as $\bar{\eta}^x$. This quantity is defined as the ratio of the mean temperature difference at the evaluated section, $T_\infty - \bar{T}^x$, to the wet bulb depression ($T_\infty - T_{wb_\infty}$).

$$\bar{\eta}^x = \frac{T_\infty - \bar{T}^x}{T_\infty - T_{wb_\infty}} \tag{13}$$

Fig. 13 shows the evaporative cooling efficiency evaluated at the outlet section of the domain, $\bar{\eta}^L$, as a function of the water-to-air mass flow ratio for all simulations performed. As can be seen, the results are scattered over a wide range: $\bar{\eta}^L = 0.146–0.712$. The maximum efficiency is obtained for the case of 36 atomisers, $v_a = 1.0$ m s^{-1}, $T_\infty = 25$ °C and $\phi_\infty = 0.7$ (simulation 7, Table 5). The lowest is observed for the case of 16 atomisers, $v_a = 1.5$ m s^{-1}, $T_\infty = 30$ °C and $\phi_\infty = 0.5$ (simulation 23, Table 5).

The trend observed for all the results is that the efficiency increases with the water-to-air mass flow ratio $\dot{m}_w/\dot{m}_a$. This is logical, since if the amount of water increases (more atomisers) and the amount of air decreases (lower v_a), the performance of evaporative cooling improves until saturation is reached. For this fact, the explanation is the same as

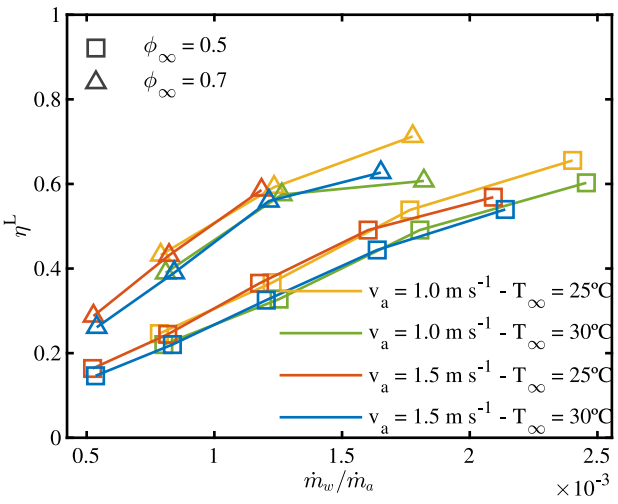

Fig. 13. Evaporative cooling efficiency as a function of the water-to-air mass flow ratio for all simulations conducted.

the one given for the results of ΔT. The relative humidity affects the wet bulb temperature and, therefore, the denominator in Eq. (13).

When the results presented in Fig. 13 are compared with those obtained in previous studies (Figure 9, [17]), it can be seen that the spray atomiser system clearly outperforms the mist generator system. The majority of the mist generator cases exhibited an evaporative efficiency value around 10%, which is the minimum value obtained by spray atomiser system. This is because with the mist generator the water injection was concentrated in a single point, which makes the evaporation process much more difficult and occurs in a very small area.

3.2.3. Percentage area at a certain temperature

The evaporative cooling efficiency is a useful measure to assess the cooling performance of the system based on the average temperature. However, it may not capture the local temperature variations. In order to compare the performance of different cases in a more quantitative way, the percentage area at a certain temperature was introduced (A_T^x). This represents the fraction of the total cross-sectional area of the tunnel where the temperature is below the specific value. For example, $A^L_{25\ °C} = 1$ means that the entire area at the outlet ($x = L$) is below 25 °C. This approach allows for a more detailed analysis of the temperature distribution and provides a more comprehensive understanding of the cooling process.

Fig. 14(a) displays the behaviour of A_T^L as a function of air temperature for several similar cases (v_a = 1.5 m s^{-1}, T_∞ = 25 °C and ϕ_∞ = 0.5) with spray atomisers and mist generator [17]. The nomenclature adopted to describe the results related to this parameter is as follows: a concave-shaped curve is observed when A_T^L drops dramatically for air temperatures around ∼ 25 °C (where T_∞ = 25 °C). This indicates that the cooled area is concentrated in a small portion of the total cross-sectional area. In Fig. 14(a), the series corresponding to the mist generator falls into this category, where the portion of the total cross-sectional area of the tunnel with temperatures lower than 25 °C is around 20% at most.

On the other hand, a convex-shaped curve represents a smoother, less steep transition for A_T^L with the temperature. The curves presented corresponds to simulations 15, 16, 17, 18 and 19 in Table 5 (16, 25, 36, 49 and 64 atomisers). As $\dot{m}_w$ increases, the air temperature approaches the wet-bulb temperature (point to which the cases of 49 and 64 atomisers tend). In the case with 25 atomisers, A_T^L values around 50% corresponds to a temperature drop of just 2 °C. However, in the case of 49 atomisers, this drop in temperature is around 4 °C. This difference is also observed in Fig. 14(b) and 14(c), the contours have a similar shape, but as $\dot{m}_w$ increases, both the temperature difference and the affected area also increase. Finally, for the case of 64 atomisers, it is observed that approximately 20% of the outlet section is close to the inlet air wet-bulb temperature. In summary, as can be seen in Fig. 14(a), the atomiser system allows greater versatility, since the spray can be distributed uniformly in the inlet section and this is reflected in the plume. It provides a tangible enhancement compared to the mist generator, since the water injection was concentrated in a single point, providing a much smaller and less uniform plume that makes the evaporation process much more difficult and increases the droplet lifetime.

3.2.4. Wet length

The last indicator discussed in this section is the wet length, L_w. The wet length is the distance from the droplet injection section until the water droplets completely evaporate. If liquid, not fully evaporated, water droplets are carried out by the airstream to the heat exchanger bundles of the condenser bundles, corrosion, scaling and fouling problems can arise.

The evolution of the wet length (or its dimensionless form, L_w/L) as a function of the water-to-air mass flow ratio is presented in Fig. 15. As it can be seen, L_w/L equals 1 in several cases with high $\dot{m}_w/\dot{m}_a$ and ϕ_∞ levels. This means that some droplets exit the domain through the outlet section, and is justified due to a reduction in the evaporation rate. As expected, low ϕ_∞ and high T_∞ levels reduce L_w/L (higher wet bulb depression).

Fig. 10 depicts, as an example, prediction of the droplets' trajectories in two representative cases. Both correspond to the conditions of T_∞ = 25 °C, ϕ_∞ = 0.5 and v_a = 1.5 m s^{-1}, Fig. 10(e) for 25 atomisers and Fig. 10(f) for 49 atomisers. As it can be seen, for the test of 25 atomisers, no droplets leave the domain, whereas for the test of 49 atomisers, there are drops that leave the domain before evaporating.

One can utilise the findings of this metric to identify the suitable ranges of $\dot{m}_w/\dot{m}_a$ that lead to a more uniform distribution of water spray and evaporation. Specifically, cases where the dimensionless wet length is less than one correspond to $\dot{m}_w/\dot{m}_a \leq 1.7 \cdot 10^{-3}$ for $\phi_\infty = 0.5$ and $\dot{m}_w/\dot{m}_a \leq 1.2 \cdot 10^{-3}$ for $\phi_\infty = 0.7$. To ensure complete evaporation of the sprayed water, it is advisable to operate within these ranges and avoid operating outside of them.

Similarly to the previously mentioned parameters, the concentrated injections in a single point generated by the mist eliminator system, also had a negative impact on the wet length, with 86% of the studied cases showing values greater than unity (liquid droplets exiting the domain).

3.3. Optimisation analysis

Based on the previous discussion, it has been emphasised that increasing the mass flow rate of water ($\dot{m}_w$) enhances the cooling efficiency, at least until saturation is attained. However, this requires the addition of more spray atomisers, which leads to increased energy consumption (1.3 W per spray atomiser). Consequently, the cooling capacity, $\dot{Q}_{\text{cooling}}$, as defined in Eq. (14), is also increased due to the temperature difference (via the cooling efficiency).

$$\dot{Q}_{\text{cooling}} = \dot{m}_a c_{p_a} \left(T_\infty - \bar{T}^L\right) \tag{14}$$

Those magnitudes can be combined into the evaporative Coefficient Of Performance (COP_{evap}), formulated in Eq. (15):

$$\text{COP}_{\text{evap}} = \frac{\dot{Q}_{\text{cooling}}}{\dot{W}_{\text{fan}} + \dot{W}_{\text{pump}} + \dot{W}_{\text{ultrasound}}} \tag{15}$$

This magnitude considers the relative contribution of all the effects mentioned above and, therefore, was selected as the key parameter to conduct an optimisation analysis. The power consumption required by the fans was calculated by using the well-known fan performance equation, Eq. (16). In other words, the theoretical consumption is

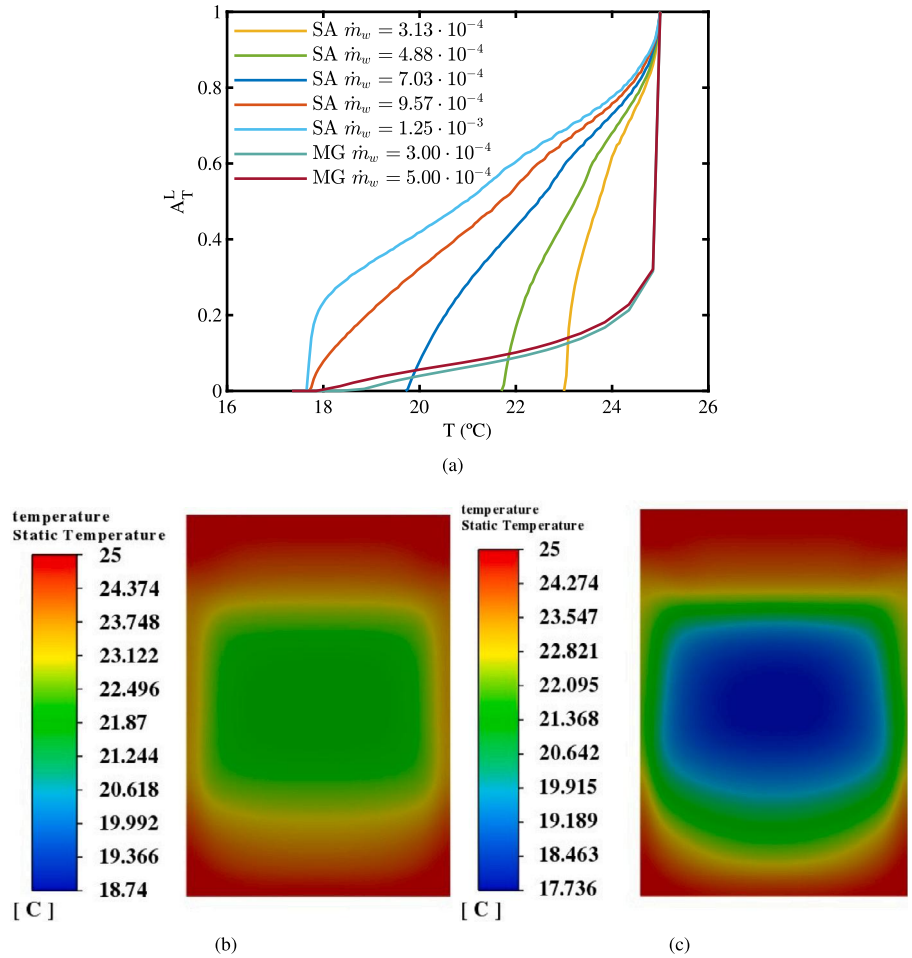

Fig. 14. (a) Variation of A_T^L as a function of the air temperature for a representative cases with the spray atomisers system and a similar case with the mist generator. Temperature contour in the outlet section of the domain for the test 16 (b) and 18 (c) in Table 5.

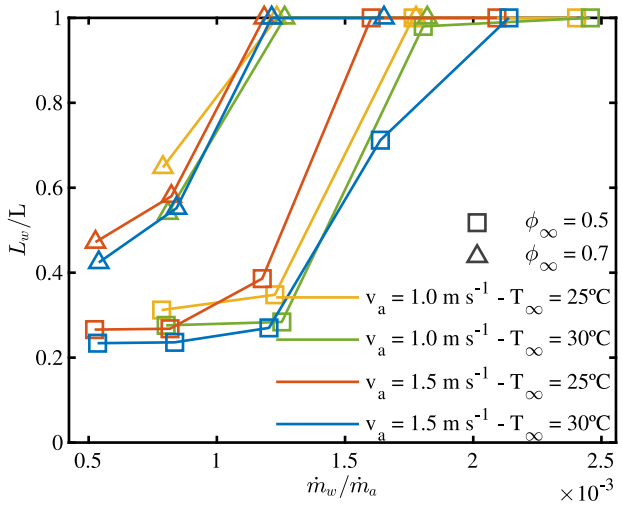

Fig. 15. Wet length (in its dimensionless form, L_w/L) as a function of water temperature for all simulations performed.

obtained with the product of the air flow rate (calculated using the measured velocity and dimensions of the wind tunnel) by the pressure loss in the tunnel. The fan efficiency was estimated at 50%. It should also be mentioned that, although it has been taken into account in this analysis, this consumption will not be present in the real application since the air flow is induced by the condenser fan.

$$\dot{W}_{\text{fan}} = \frac{Q\Delta p}{\eta_f} \tag{16}$$

The power consumption of the ultrasonic spray atomisers and the pump was experimentally measured. It was observed that it was not affected by the operating conditions. Observed values of 1.3 W and 5 W were considered in the calculations for the atomisers and the pump, respectively.

Fig. 16 illustrates the impact of $\dot{m}_w/\dot{m}_a$ on COP_{evap} for all simulations carried out. The atomiser system is responsible for the majority of power consumption, accounting for approximately 79%–94% of the total. The pump, which recirculates the sprayed water, consumes the remaining power. The theoretical power required to generate the primary airflow is negligible compared to these other power uses. Thus, the COP_{evap} values are primarily influenced by $\dot{m}_w$.

The general trend observed is that COP_{evap} first increases with $\dot{m}_w/\dot{m}_a$ until an optimum is reached, and then decreases. Increasing COP_{evap} values can be explained because the temperature drop effect (increased evaporation rate) overcomes the power consumption in Eq. (15). At some point, increasing the number of atomisers does not favour evaporation (saturation is reached) and COP_{evap} decreases. The maximum value of the COP_{evap} is 30.49, which is obtained for the case of 49 atomisers, $v_a = 1.5$ m s^{-1}, $T_\infty = 25$ °C and $\phi_\infty = 0.5$. It is observed that the COP_{evap} decreases from $\dot{m}_w/\dot{m}_a < 1.8 \cdot 10^{-3}$ for $\phi_\infty = 0.5$, and from $\dot{m}_w/\dot{m}_a < 8.1 \cdot 10^{-4}$ for $\phi_\infty = 0.7$. Within this range, the optimal trade-off between cooling capacity and power consumption is achieved. Additionally, these ranges align with the operational ranges that result

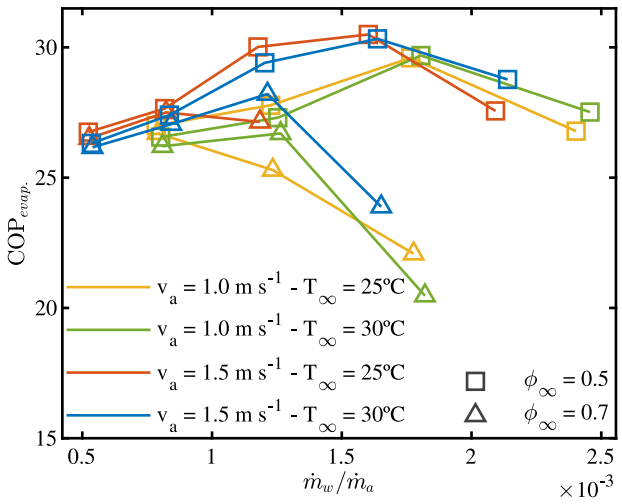

Fig. 16. Coefficient of performance as a function of the water-to-air mass flow ratio for all the simulations conducted.

in the most effective wet length. Thus, the benefits of operating within these ranges are twofold.

This is also a key differential factor with respect to the mist generator, since for this system the COP fluctuated between 2.4 and 7. This difference can be explained by the higher power consumption of the device (200 W) alongside the lower evaporative performance.

4. Conclusions

In this study, a numerical model of an ultrasonic atomiser system for evaporative pre-cooling of condenser inlet air in air conditioning applications has been developed. The accuracy of the model was confirmed through experimental tests. Once validated, the model was used to investigate the physical variables affecting the cooling process, including the number and distribution of injections, air speed, temperature, and humidity. Finally, the optimal operating point was obtained for each set of simulations carried out with respect to the overall performance of all systems involved in the cooling process. This is the summary of the conclusions obtained in this work:

- The average efficiency of evaporative cooling at the domain outlet, $\bar{\eta}^L$, increases with higher water-to-air mass flow ratios ($\dot{m}_w/\dot{m}_a$), temperature, and humidity. This statement is valid until air saturation is reached. The highest value of $\bar{\eta}^L = 0.712$ is observed for a setup with 36 atomisers, an air velocity of 1.0 m s^{-1}, an ambient temperature of 25 °C, and a relative humidity of 0.7.
- The wet length was studied in order to know the operating ranges where the plume is more homogeneous, since this promotes evaporation and avoids liquid drops hitting the condenser. These ranges are $\dot{m}_w/\dot{m}_a \leq 1.7 \cdot 10^{-3}$ for $\phi_\infty = 0.5$ and $\dot{m}_w/\dot{m}_a \leq 1.2 \cdot 10^{-3}$ for $\phi_\infty = 0.7$.
- The optimisation analysis based on the evaporative coefficient of performance has shown that the operating ranges that show better overall performance are $\dot{m}_w/\dot{m}_a < 1.8 \cdot 10^{-3}$ for $\phi_\infty = 0.5$, and from $\dot{m}_w/\dot{m}_a < 8.1 \cdot 10^{-4}$ for $\phi_\infty = 0.7$. To calculate the total power, the consumption of each atomiser has been considered, in addition to the rest of the constant consumption of the installation (recirculation pump and fan). Therefore, if the number of atomisers is increased, $\dot{m}_w$ is increased proportionally and the performance is distributed over the fixed consumption of the system. This happens as long as the complete evaporation of practically all the drops takes place. When this changes, system performance drops dramatically.

The results obtained reveal the high potential of ultrasonic spray atomiser systems, since the limitations of the ultrasonic devices studied previously have been overcome. The spray atomiser system allows a simpler regulation of the plume distribution and improves the practical operation (wet length) as well as the performance.

CRediT authorship contribution statement

P. Navarro: Software, Investigation, Formal analysis, Investigation, Data curation, Writing – original draft, Writing – review & editing. **J. Ruiz:** Methodology, Software, Formal analysis, Investigation, Writing – original draft, Writing – review & editing, Project administration, Funding acquisition. **P. Martínez:** Conceptualization, Data curation, Writing – review & editing, Supervision, Funding acquisition. **M. Lucas:** Conceptualization, Writing – review & editing, Supervision, Project administration, Funding acquisition.

Declaration of competing interest

The authors declare that they have no known competing financial interests or personal relationships that could have appeared to influence the work reported in this paper.

Data availability

Data will be made available on request.

Acknowledgements

The authors acknowledge the financial support received from the Government of Valencia (Generalitat Valenciana), Spain, through project AICO/2021/190 (Subvenciones para grupos de investigación consolidables).

References

[1] S. He, Z. Guan, H. Gurgenci, K. Hooman, Y. Lu, A.M. Alkhedhair, Experimental study of the application of two trickle media for inlet air pre-cooling of natural draft dry cooling towers, Energy Convers. Manage. 89 (2015) 644–654, http://dx.doi.org/10.1016/j.enconman.2014.10.031, URL https://www.sciencedirect.com/science/article/pii/S0196890414009121.

[2] S. He, Y. Xu, G. Zhang, K. Hooman, M. Gao, Selection of wetted media for pre-cooling of air entering natural draft dry cooling towers, Appl. Therm. Eng. 114 (2017) 857–863, http://dx.doi.org/10.1016/j.applthermaleng.2016.11.179, URL https://www.sciencedirect.com/science/article/pii/S135943111632018X.

[3] M. Yan, S. He, N. Li, X. Huang, M. Gao, M. Xu, J. Miao, Y. Lu, K. Hooman, J. Che, Z. Geng, S. Zhang, Experimental investigation on a novel arrangement of wet medium for evaporative cooling of air, Int. J. Refrig. 124 (2021) 64–74, http://dx.doi.org/10.1016/j.ijrefrig.2020.12.014, URL https://www.sciencedirect.com/science/article/pii/S0140700720305089.

[4] P. Martínez, J. Ruiz, C. Cutillas, P. Martínez, A. Kaiser, M. Lucas, Experimental study on energy performance of a split air-conditioner by using variable thickness evaporative cooling pads coupled to the condenser, Appl. Therm. Eng. 105 (2016) 1041–1050, http://dx.doi.org/10.1016/j.applthermaleng.2016.01.067, URL http://www.sciencedirect.com/science/article/pii/S1359431116300175.

[5] N.I. Ibrahim, A.A. Al-Farayedhi, P. Gandhidasan, Experimental investigation of a vapor compression system with condenser air pre-cooling by condensate, Appl. Therm. Eng. 110 (2017) 1255–1263, http://dx.doi.org/10.1016/j.applthermaleng.2016.09.042, URL http://www.sciencedirect.com/science/article/pii/S1359431116316386.

[6] S. Kumar, S.S. Salins, P.S. Nair, A. Tejero-González, Parametric evaluation of dynamic multistage centrifugal humidifier, J. Build. Eng. 62 (2022) 105305, http://dx.doi.org/10.1016/j.jobe.2022.105305, URL https://www.sciencedirect.com/science/article/pii/S2352710222013110.

[7] A. Alkhedhair, H. Gurgenci, I. Jahn, Z. Guan, S. He, Numerical simulation of water spray for pre-cooling of inlet air in natural draft dry cooling towers, Appl. Therm. Eng. 61 (2) (2013) 416–424, http://dx.doi.org/10.1016/j.applthermaleng.2013.08.012, URL http://www.sciencedirect.com/science/article/pii/S135943111300584X.

[8] H. Montazeri, B. Blocken, J. Hensen, Evaporative cooling by water spray systems: CFD simulation, experimental validation and sensitivity analysis, Build. Environ. 83 (2015) 129–141, http://dx.doi.org/10.1016/j.buildenv.2014.03.022, URL http://www.sciencedirect.com/science/article/pii/S0360132314000821, Special Issue: Climate adaptation in cities.

[9] M. Sadafi, J. Ruiz, M. Lucas, I. Jahn, K. Hooman, Numerical and experimental study on a single cone saline water spray in a wind tunnel, Int. J. Therm. Sci. 120 (2017) 190–202, URL http://www.sciencedirect.com/science/article/pii/S129007291631537X.

[10] J. Tissot, P. Boulet, F. Trinquet, L. Fournaison, H. Macchi-Tejeda, Air cooling by evaporating droplets in the upward flow of a condenser, Int. J. Therm. Sci. 50 (11) (2011) 2122–2131, http://dx.doi.org/10.1016/j.ijthermalsci.2011.06.004, URL http://www.sciencedirect.com/science/article/pii/S1290072911001815.

[11] F. Raoult, S. Lacour, B. Carissimo, F. Trinquet, A. Delahaye, L. Fournaison, CFD water spray model development and physical parameter study on the evaporative cooling, Appl. Therm. Eng. 149 (2019) 960–974, http://dx.doi.org/10.1016/j.applthermaleng.2018.12.063, URL https://www.sciencedirect.com/science/article/pii/S1359431118327686.

[12] Y. Hou, Y. Tao, X. Huai, Z. Guo, Numerical characterization of multi-nozzle spray cooling, Appl. Therm. Eng. 39 (2012) 163–170, http://dx.doi.org/10.1016/j.applthermaleng.2012.01.030, URL http://www.sciencedirect.com/science/article/pii/S1359431112000324.

[13] K.D. Kim, D.H. Jin, Y.C. Choi, Numerical simulation on the generation of ultrasound and formation of water fog in the ultrasonic gas atomizer, Ultrasonics 102 (2020) 105851, http://dx.doi.org/10.1016/j.ultras.2018.11.002, URL http://www.sciencedirect.com/science/article/pii/S0041624X18301586.

[14] Y. Yao, Research and applications of ultrasound in HVAC field: A review, Renew. Sustain. Energy Rev. 58 (2016) 52–68, http://dx.doi.org/10.1016/j.rser.2015.12.222, URL http://www.sciencedirect.com/science/article/pii/S1364032115016056.

[15] Y. Yao, Y. Pan, S. Liu, Power ultrasound and its applications: A state-of-the-art review, Ultrasonics Sonochemistry 62 (2020) 104722, http://dx.doi.org/10.1016/j.ultsonch.2019.104722, URL http://www.sciencedirect.com/science/article/pii/S1350417719308995.

[16] P. Martínez, J. Ruiz, I. Martín, M. Lucas, Experimental study of an ultrasonic mist generator as an evaporative cooler, Appl. Therm. Eng. 181 (2020) 116057, http://dx.doi.org/10.1016/j.applthermaleng.2020.116057, URL https://www.sciencedirect.com/science/article/pii/S1359431120335377.

[17] J. Ruiz, P. Martínez, I. Martín, M. Lucas, Numerical characterization of an ultrasonic mist generator as an evaporative cooler, Energies 13 (11) (2020) http://dx.doi.org/10.3390/en13112971, URL https://www.mdpi.com/1996-1073/13/11/2971.

[18] J. Ruiz, Experimental Characterization and Modelling of the Binomial Distribution System-Drift Eliminator in Cooling Towers (Ph.D. thesis), Technical University of Cartagena, 2014.

[19] P. Martínez, J. Ruiz, P. Martínez, A. Kaiser, M. Lucas, Experimental study of the energy and exergy performance of a plastic mesh evaporative pad used in air conditioning applications, Appl. Therm. Eng. 138 (2018) 675–685, http://dx.doi.org/10.1016/j.applthermaleng.2018.04.065, URL http://www.sciencedirect.com/science/article/pii/S1359431117378225.

[20] J. Ruiz, C. Cutillas, A. Kaiser, B. Zamora, H. Sadafi, M. Lucas, Experimental study on pressure loss and collection efficiency of drift eliminators, Appl. Therm. Eng. 149 (2019) 94–104, http://dx.doi.org/10.1016/j.applthermaleng.2018.12.023, URL http://www.sciencedirect.com/science/article/pii/S1359431118355388.

[21] K.A. Ramisetty, A.B. Pandit, P.R. Gogate, Investigations into ultrasound induced atomization, Ultrasonics Sonochemistry 20 (1) (2013) 254–264, http://dx.doi.org/10.1016/j.ultsonch.2012.05.001, URL https://www.sciencedirect.com/science/article/pii/S1350417712000909.

[22] M. Sadafi, I. Jahn, K. Hooman, Nozzle arrangement effect on cooling performance of saline water spray cooling, Appl. Therm. Eng. 105 (2016) 1061–1066, http://dx.doi.org/10.1016/j.applthermaleng.2016.01.078, URL http://www.sciencedirect.com/science/article/pii/S135943111630028X.

[23] A. Alkhedhair, I. Jahn, H. Gurgenci, Z. Guan, S. He, Y. Lu, Numerical simulation of water spray in natural draft dry cooling towers with a new nozzle representation approach, Appl. Therm. Eng. 98 (2016) 924–935, http://dx.doi.org/10.1016/j.applthermaleng.2015.10.118, URL http://www.sciencedirect.com/science/article/pii/S1359431115011771.

[24] Z. Zhang, S. He, M. Yan, M. Gao, Y. Shi, Y. Lu, J. Liu, C. Guo, X. Huang, Numerical study on the performance of a two-nozzle spray cooling system under different conditions, Int. J. Therm. Sci. 152 (2020) 106291, http://dx.doi.org/10.1016/j.ijthermalsci.2020.106291, URL http://www.sciencedirect.com/science/article/pii/S1290072919317685.

[25] S.A. Morsi, A.J. Alexander, An investigation of particle trajectories in two-phase flow systems, J. Fluid Mech. 55 (2) (1972) 193–208, http://dx.doi.org/10.1017/S0022112072001806.

[26] W.E. Ranz, W.R. Marshall, Evaporation from drops Part I, Chem. Eng. Prog. 48 (3) (1952) 141–146.

[27] W.E. Ranz, W.R. Marshall, Evaporation from drops Part II, Chem. Eng. Prog. 48 (4) (1952) 173–180.

[28] J. Ruiz, A. Kaiser, B. Zamora, C. Cutillas, M. Lucas, CFD analysis of drift eliminators using RANS and LES turbulent models, Appl. Therm. Eng. 105 (2016) 979–987, http://dx.doi.org/10.1016/j.applthermaleng.2016.01.108, URL http://www.sciencedirect.com/science/article/pii/S1359431116300588.

[29] Ansys fluent ©Academic research, ansys fluent 21, 2021, https://www.ansys.com.

[30] P.J. Roache, Computational Fluid Dynamics, Hermosa Publishers, Albuquerque, 1972, 446 p : ill, 27 cm, URL http://infoscience.epfl.ch/record/60253.